



# HgCdTe Films Grown by MBE on CZT(211)B Substrates

G. Qin<sup>1</sup> · J. C. Kong<sup>1</sup> · J. Yang<sup>1</sup> · Y. Ren<sup>1</sup> · Y. H. Li<sup>1</sup> · C. Z. Yang<sup>1</sup> · H. F. Li<sup>1</sup> · J. Y. Wang<sup>1</sup> · J. Y. Yu<sup>1</sup> · Q. Qin<sup>1</sup> · J. Zhao<sup>1</sup> · P. Zhao<sup>1</sup>

Received: 14 September 2022 / Accepted: 20 December 2022 / Published online: 25 January 2023  
© The Minerals, Metals & Materials Society 2023

## Abstract

An investigation of the properties of HgCdTe films grown by MBE and devices made from such films are reported. Through the precise control of growth conditions and the screening of the Zn component of CZT(211)B substrates, high-quality HgCdTe films were successfully deposited onto the CZT(211)B substrates and characterized by x-ray diffraction rocking curve analysis and etch pit density analysis. X-ray rocking curve (422) reflection full-width at half-maximum (FWHM) of less than 15 arcsec was obtained for Hg<sub>0.7</sub>Cd<sub>0.3</sub>Te epitaxial films, and etch pit density (EPD) of about  $2 \times 10^4 \text{ cm}^{-2}$  was observed. At the same time, the relationship between the FWHM of the x-ray double-crystal rocking curve and EPD was confirmed. By optimizing the pretreatment process of the CZT(211)B substrate, a further significant reduction in HgCdTe macrodefect densities to  $54 \text{ cm}^{-2}$  to  $1000 \text{ cm}^{-2}$  was observed on CdZnTe, including occasional occurrences of very few or no large "void clusters" that are often observed. Planar p-on-n HgCdTe mid-wave infrared (MWIR) focal plane arrays (FPAs) were fabricated based on MBE in situ indium doping and arsenic ion implantation technology. The temperature-dependent performance of planar p-on-n MWIR FPAs shows that the device has the ability to operate at high temperature of about 140 K with high performance.

**Keywords** MBE · HgCdTe films · crystal quality · MWIR FPAs · temperature-dependent performance

## Introduction

Hg<sub>1-x</sub>Cd<sub>x</sub>Te (MCT) material, invented by British scientists Lawson and co-workers in 1959, is a ternary compound semiconductor. By adjusting the cadmium component, the infrared detection of three atmospheric windows of 1–3 μm, 3–5 μm and 8–14 μm can be realized. The HgCdTe photon detector has the advantage of high quantum efficiency (QE) because of its direct bandgap and large absorption coefficient, and is in the leading position for application in the field of high-performance cooled infrared photon detectors due to its excellent photoelectric performance. The HgCdTe detector is the core device with the most urgent demand and the most extensive applications in high-performance infrared photoelectric systems such as photoelectric imaging, radar

early warning, air defense, anti-missile, and space remote sensing detection.<sup>1–4</sup>

At present, HgCdTe infrared detectors are developing towards a new generation of infrared detector technology called SWaP<sup>3</sup>, and high-quality thin film materials are the basis for the development of high-performance infrared detectors. Molecular beam epitaxy (MBE) technology has the advantages of an ultra-high vacuum growth environment, flexible in situ doping, steep interface control and multilayer heterojunction growth. It is one of the most promising "flexible" manufacturing technologies for the development of new-generation HgCdTe infrared focal plane arrays (FPAs), such as HgCdTe multicolor and HOT detectors.<sup>3–11</sup>

Cd<sub>1-y</sub>Zn<sub>y</sub>Te (CZT) material can achieve perfect lattice matching with HgCdTe material by adjusting the zinc component, which is an ideal substrate for the epitaxial growth of high-quality HgCdTe films.<sup>12</sup> This paper studies the properties of HgCdTe films grown by MBE on CZT(211)B substrate. Based on this, a planar p-on-n mid-wave infrared HgCdTe FPA is fabricated and its performance is verified.

✉ J. C. Kong  
kongjincheng@163.com

G. Qin  
qingang0125@163.com

<sup>1</sup> Kunming Institute of Physics, Kunming 650223, Yunnan, China

## Experiment

The polished CZT substrate is corroded with 0.5% bromine methanol for 10 s, cleaned by deionized water, and then fixed on the molybdenum sample holder with indium bonding. The growth is performed in a Riber 32P MBE system equipped with a liquid Hg source, a reflection high-energy electron diffraction (RHEED) system, and an infrared pyrometer. The growth temperature is well controlled by proportional–integral–differential (PID) feedback via a Ga-wetted thermocouple in direct contact with the sample holder. The surface oxide layer on the substrate is removed by deoxidizing at 320°C for 5 min, and then the HgCdTe film is grown at the optimal growth temperature of  $180 \pm 1^\circ\text{C}$ . The deoxidization and growth processes are real-time monitored by in situ RHEED.

A Fourier-transform infrared (FTIR) spectrometer was used for transmission spectroscopy. Transmission spectroscopy was used to determine the composition and thickness of the HgCdTe layers. The crystal quality of the grown HgCdTe films is assessed by the full-width at half-maximum (FWHM) of the x-ray double-crystal rocking curve (DCRC). Analysis of threading dislocation densities measured by etch pit density (EPD) using published Schaake and Chen etchants<sup>13–15</sup> for HgCdTe films with pit counting and evaluation of the distribution is performed with an optical microscope at  $\times 1000$  magnification. The surface macrodefect density is counted by a metallographic microscope at  $\times 50$  magnification, and the origin of macrodefects on the surface of HgCdTe films is analyzed by scanning electron microscopy (SEM).

Planar p-on-n HgCdTe mid-wave infrared (MWIR) FPAs based on MBE-grown in situ indium-doped HgCdTe films with thickness of 7–8  $\mu\text{m}$  are fabricated by arsenic ion implantation, and the temperature-dependent performance of devices is tested and analyzed.

## Results and Discussion

### Material Crystal Quality

Because of the narrow growth window ( $180 \pm 1^\circ\text{C}$ ) for HgCdTe films grown by MBE, the precise control of the growth temperature directly restricts the crystal quality of HgCdTe epitaxial films. The growth temperature is good controlled by PID feedback via a Ga-wetted thermocouple in direct contact with the sample holder. Figure 1 shows the RHEED patterns of material grown with different time, indicating that the growth mechanism of HgCdTe films has rapidly changed into two-dimensional growth.

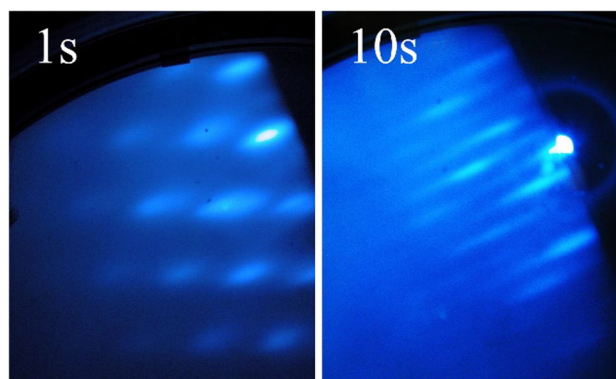


Fig. 1 RHEED patterns at the initial stage of HgCdTe growth.

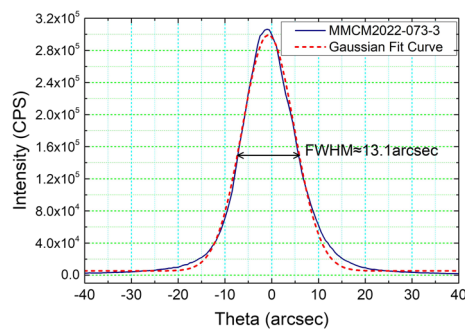


Fig. 2 The x-ray rocking curve of mid-wave HgCdTe film.

The minimum value of DCRC-FWHM of HgCdTe films is less than 15 arcsec, which is equivalent to the international advanced level such as that reported by TIS and RVS in the USA.<sup>16–20</sup> Figure 2 displays a typical x-ray rocking curve for the (422) reflection for  $\text{Hg}_{0.7}\text{Cd}_{0.3}\text{Te}$  films deposited on CZT substrates, and the FWHM is about 13.1 arcsec. The results show that the HgCdTe films have good crystal quality, and there is no obvious dislocation proliferation in the HgCdTe epitaxial layer compared with the CZT(211)B substrate.

Threading dislocations are typically observed in HgCdTe epitaxial layers by the application of a decorative defect etch to reveal an etch pit density (EPD).<sup>21–24</sup> According to a large number of experimental statistics of HgCdTe films, it is further confirmed that the corresponding relationship between EPD and FWHM of the x-ray diffraction (XRD) rocking curves of HgCdTe films grown by MBE on CZT(211)B substrate is consistent with that reported in the literature,<sup>18</sup> as shown in Fig. 3.

According to the statistical results, the main reason for the large dispersion of EPD of HgCdTe films is the dispersion of the zinc component of the CZT(211)B substrate. Thus, screening the zinc component of CZT substrates is the basis for the epitaxial growth of high-quality HgCdTe films. Figure 4 shows the EPD distribution and dislocation

density of HgCdTe films under  $\times 1000$  optical microscope, and the corresponding XRD FWHM and Zn components are also marked in the figure. In consideration of space, only six combined diagrams are placed in Fig. 4 to represent the dislocation etch pit distribution on the surface of a thin film, especially grown on a CZT(211)B substrate with a large dispersion of Zn component distribution, or different thin films grown on CZT(211)B substrates with different Zn components. It should be noted that mainly single etch pits are uniformly distributed across the film, but a few small clusters are visible.

Etch pits are counted by recording up to 12 micrographs (each image covering an area of  $105.03 \mu\text{m} \times 59.03 \mu\text{m}$ ) and counting the etch pits manually. The actual number of images used for a particular sample is chosen according to the etch pit density to ensure good counting statistics.

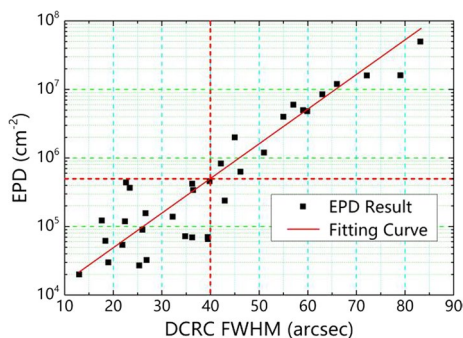


**Fig. 3** Corresponding relationship between EPD and DCRC-FWHM of HgCdTe films (the thickness of MCT films ranges from 8 to  $10 \mu\text{m}$ ).

For counting of the small etch pits, images with higher magnification ( $\times 1000$ ) are recorded.

Based on the dark current and noise mechanism of HgCdTe detectors, in order to realize the fabrication of high-performance infrared detectors, especially for long-wave infrared (LWIR) and very-long-wave infrared (VLWIR) detectors, it is necessary to ensure that the threading dislocation density of HgCdTe films is typically less than  $5 \times 10^5 \text{ cm}^{-2}$ .<sup>21</sup> According to the fitting curve of the relationship between EPD and DCRC-FWHM of HgCdTe films shown in Fig. 4, the DCRC-FWHM of HgCdTe films should be controlled within 40 arcsec.

### Surface Macrodefects

The macrodefect density on the surface of HgCdTe films directly affects the number of defective pixels of FPAs.<sup>25,26</sup> Here, pixels were defined as defective when individual noise equivalent temperature difference (NETD) or temporal noise exceeds  $\pm 100\%$  of the mean value of all pixels or if its response is less than 0.7 or larger than 1.3 times the mean response. The relatively low macrodefect density is the basis for high performance of HgCdTe devices. Macrodefect density consists of all defects on HgCdTe epitaxial layers that can be viewed under an optical microscope. Therefore, the macrodefects include micro-voids, voids, spits, and other defects.

The surface macrodefects of HgCdTe films can be classified into two categories; one is related to the growth conditions, such as growth temperature and flux ratio, and the other is related to the surface state of the polished CZT substrate.<sup>27</sup> The macrodefects related to growth conditions

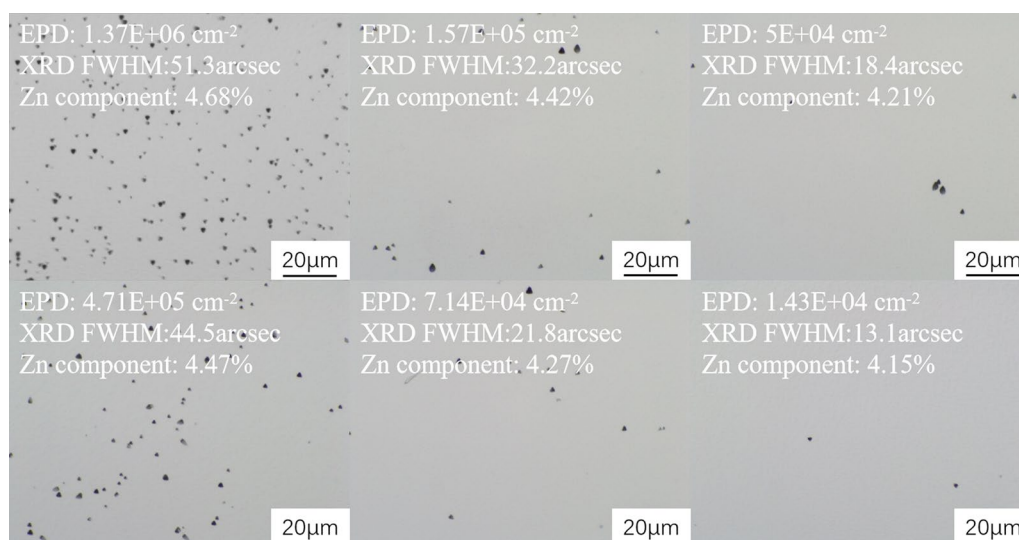


**Fig. 4** The EPD distribution and dislocation density of HgCdTe films under  $\times 1000$  optical microscope, and the corresponding DCRC-FWHM and Zn components are also marked.

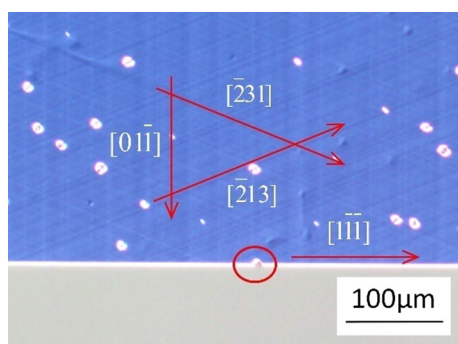


**Fig. 5** Surface morphology and macrodefects of HgCdTe films.

can be effectively eliminated by good growth temperature control and precise adjustment of Hg/Te flux ratio so that the surface macrodefects mainly come from the surface state of CZT(211)B substrate after polishing or corrosion. Figure 5 shows the typical morphology of HgCdTe films grown on CZT(211)B substrate by MBE, and the size of surface macrodefects is mainly distributed in the range of 4–7  $\mu\text{m}$ . A well-defined surface cross-hatch pattern resulting from the growth modulation caused by the lattice-mismatch between HgCdTe films and CZT(211)B substrate is observed, reflecting that the MBE growth technique of HgCdTe film has high maturity.<sup>28–30</sup>

Macrodefects can generally be observed on the surface of MBE-grown HgCdTe films on CZT(211)B substrate, with a substantial fraction believed to arise from defective growth on telluride precipitates present on the CZT(211)B substrate surface. In addition, the microparticle residues on the surface of CZT substrate are also an important origin of macrodefects, especially for the "void cluster" defects.<sup>30–34</sup>

In order to reduce the macrodefect density on the surface of the HgCdTe films, it is necessary to identify the origin of the surface macrodefects of our grown films. The sample is cleaved along the  $(0\bar{1}1)$  face, and the morphology of the cleavage plane is observed by SEM. The cross-sectional SEM image of HgCdTe sample cleaved along the  $(0\bar{1}1)$  face is shown in Fig. 6, and a V-shaped macrodefect is noted in the HgCdTe film.

According to the cross-sectional SEM image of the surface macrodefect, we hypothesized that the surface macrodefects might be caused by the microparticles remaining on the surface of the polished or corroded CZT substrate. Based on this hypothesis, energy-dispersive x-ray spectroscopy (EDX) is used to investigate the elements of microparticle residues on the surface of the pretreated substrates. The results obtained from EDX analysis of the microparticle residues reveal the presence of the elements Zn, Al, Cd, Te, Si and O, as shown in Fig. 7a and b. Oxygen is detected indirectly by both systems, thereby

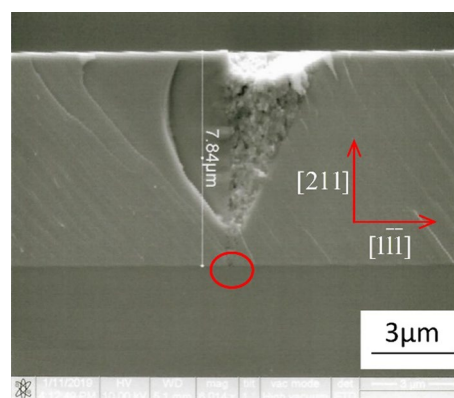


**Fig. 6** The cross-sectional SEM image of the cleavage plane of HgCdTe film.

indicating that the elements in the sample may be present in the form of their metal oxides, namely  $\text{SiO}_2$  and  $\text{Al}_2\text{O}_3$ , introduced from the substrate pretreatment process.

After confirming the main origin of surface macrodefects, the optimization experiments of substrate pretreatment process are carried out to solve the problem of residual particles on the substrate surface, including ultrasonic cleaning, HF acid corrosion cleaning and optimization of grinding and polishing process.

By further optimizing the substrate pretreatment process, the macrodefect density on the surface of the HgCdTe films can be effectively reduced. Macrodefects are counted by recording up to twelve micrographs (each image covering an area of  $2100.67 \mu\text{m} \times 1180.67 \mu\text{m}$ ) and counting the defects manually. The actual number of images used for a particular sample is chosen according to the macrodefect density to ensure good counting statistics. For counting of the larger voids, images with lower magnification ( $\times 50$ ) are recorded.

The macrodefect density is very uniform on the wafers and the minimum density reached  $54 \text{ cm}^{-2}$ , and the statistical average value is less than the target value of  $1000 \text{ cm}^{-2}$ . At present, the macrodefect density of MCT materials with a thickness range of 8–10  $\mu\text{m}$  grown by MBE in our institution is comparable to that reported by TIS and RVS,<sup>16–20</sup> and run-to-run reproducibility is very good. Figure 8 shows the surface morphology of HgCdTe films grown after the optimization of substrate pretreatment process. Figure 9 shows the macrodefect density and the reproducibility of the macrodefect density of a series of sequentially MBE-grown HgCdTe films, after optimizing the pretreatment process of CZT(211)B substrate. These results indicate that the surface macrodefects that originated from the microparticles remaining on the surface of CZT(211)B substrates are effectively suppressed.

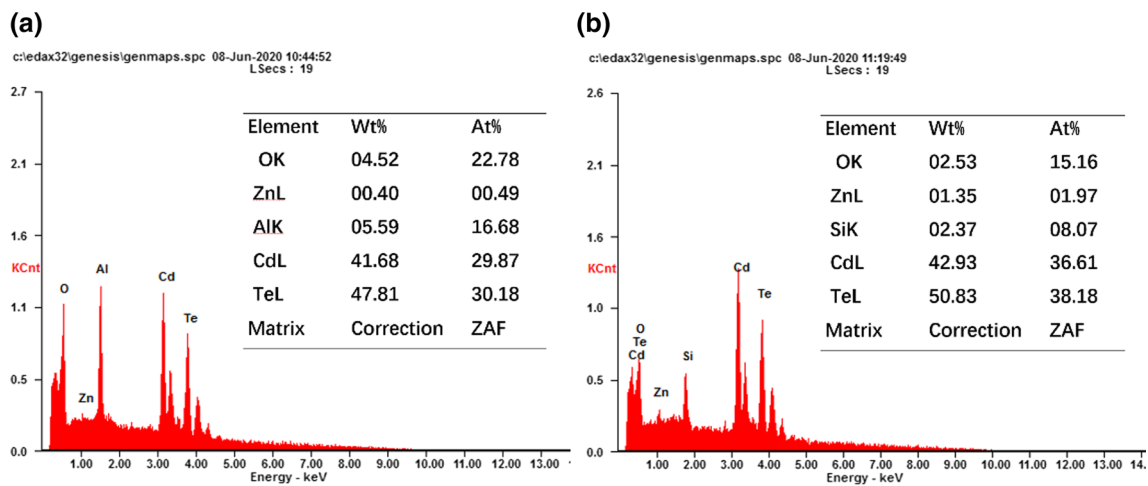


Fig. 7 Both a and b show the EDX results of microparticle residues on pretreated CZT substrate.

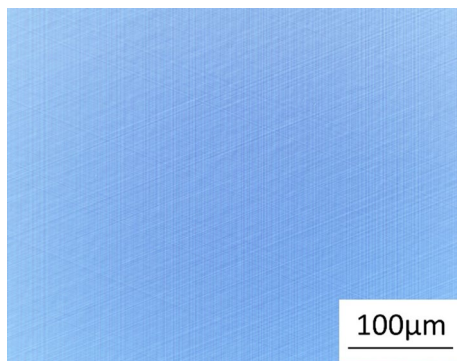


Fig. 8 Surface morphology of HgCdTe films grown after the optimization of substrate pretreatment.

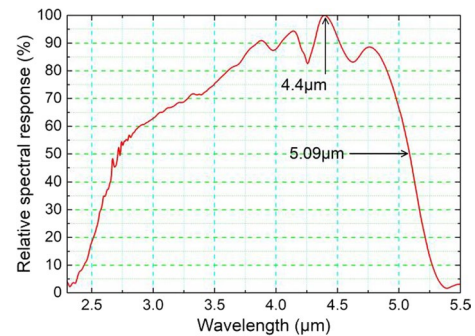


Fig. 10 Relative spectral response of MWIR HgCdTe FPAs at 77 K.

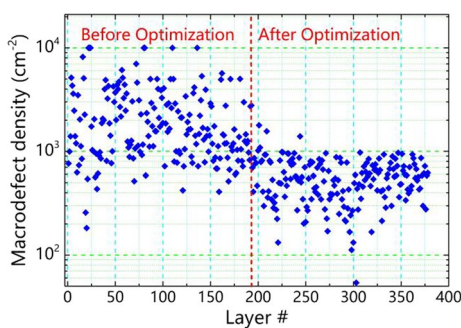


Fig. 9 The macrodefect density and the reproducibility of the macrodefect density of a series of sequentially MBE-grown HgCdTe films after the optimization of substrate pretreatment.

### Fabrication and Performance of MWIR FPAs

A 7.5- $\mu\text{m}$ -thick MWIR HgCdTe ( $x=0.30$ ) film is grown on CZT(211)B substrate by a Riber 32P MBE system, with an

indium doping concentration of about  $5 \times 10^{14} \text{ cm}^{-3}$ . The  $640 \times 512$  MWIR HgCdTe FPAs with a pixel pitch of  $15 \mu\text{m}$  are fabricated with planar p-on-n junctions achieved by arsenic implantation into an indium-doped HgCdTe base layer. The HgCdTe chip arrays and column-level analog-to-digital converter (ADC) digital silicon readout integrated circuit (ROIC) are interconnected to hybrid FPAs by flip-chip bonding using indium bumps, and then packaged into the testing Dewar ( $F\# = 2$ ). The performance of MWIR HgCdTe FPAs at 77 K is studied. Figure 10 shows the relative spectral response curve of MWIR HgCdTe FPA. Figure 11 shows the thermal response pixel mapping for a MWIR HgCdTe FPA presented in front of a 293 K blackbody.

The NETD value for the fabricated FPA measured at 77 K is about 10mK. The NETD of the IR FPA can be calculated according to the formula:<sup>35</sup>

$$\text{NETD} = \frac{[1 + (J_d/J_\Phi)]}{\eta_{cs} C \sqrt{(J_d + J_\Phi)} A \tau_{\text{int}} / q} \quad (1)$$



**Fig. 11** Thermal response pixel mapping attained for a 293 K black-body screen illumination for a MWIR HgCdTe FPA operated at 77 K.

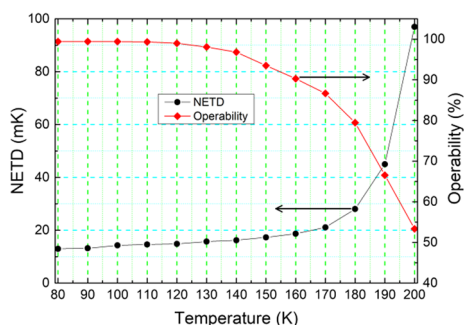


**Fig. 12** Temperature-dependent NETD and operability of MWIR HgCdTe FPA.

where  $J_d$  is the dark current density,  $J_\phi$  is the background flux current,  $C = (d\Phi_B/dT)/\Phi_B$  is the scene contrast through the optics,  $\Phi_B$  is the flux from the cold shield,  $A$  is the pixel area,  $\tau_{int}$  is the available integration time,  $\eta_{cs}$  is the cold shield efficiency, and  $q$  is the electron charge. At 77 K,  $J_d = 0$  and  $\eta_{cs} = 1$ .<sup>35</sup> The calculation of NETD shows that the noise of the FPA at 77 K is dominated by the shot noise caused by the background photon. The operability of the FPA is 99.496%, and the center size of  $320 \times 256$  is 99.662%. The operability is defined as the number of pixels with a NETD value or temporal noise within  $\pm 100\%$  of the mean value of all pixels, or the number of pixels with responsivity value within  $\pm 30\%$  of the mean. The photoreponse non-uniformity of the FPA is 4.08%. These results show that the planar p-on-n MWIR HgCdTe FPA has excellent performance.

The temperature-dependent performance of the FPAs is tested. Figure 12 shows the NETD and operability of MWIR HgCdTe FPA as a function of temperature.

According to the temperature-dependent performance results of MWIR HgCdTe FPA, the NETD increases rapidly

with the increase of temperature when the operating temperature is above 170 K. The variation trend of NETD with temperature is consistent with that of p-on-n HgCdTe mid-wave infrared FPAs reported by AIM in Germany and Sofradir in France.<sup>36,37</sup> The operability of MWIR HgCdTe FPA decreases significantly with the increase of temperature when the operating temperature is above 140 K. The temperature-dependent performance shows that planar p-on-n MWIR HgCdTe FPAs have the ability of operating temperature of about 140 K, which indicates that the HgCdTe films grown on CZT(211)B substrate by MBE have high crystal quality.

## Conclusions

High-quality HgCdTe films are grown on CZT(211)B substrates by MBE. Layers having specular surface morphology, good crystalline structure, and surface macrodefect densities  $< 1000 \text{ cm}^{-2}$  are routinely achieved, and run-to-run reproducibility is very good. The minimum value of DCRC-FWHM of HgCdTe films is less than 15 arcsec, and the EPD is about  $2 \times 10^4 \text{ cm}^{-2}$ . The quality parameters of HgCdTe films are comparable to the international advanced level, but there are still some gaps. The corresponding relationship between EPD and DCRC-FWHM reported in the relevant literature is further confirmed.

Planar p-on-n MWIR HgCdTe FPAs are fabricated based on MBE-grown in situ indium-doped HgCdTe films with the thickness of 7–8  $\mu\text{m}$  using an arsenic implantation technique. We have demonstrated high-performance MWIR  $640 \times 512$  HgCdTe FPAs and found that the FPAs still have high performance at operating temperatures of approximately 140 K. The MBE growth technology of high-quality HgCdTe films on CZT(211)B substrate provides a very important basis for the fabrication of a new generation of high-performance HgCdTe infrared detectors currently under development at the Kunming Institute of Physics, such as NPN MW/LW dual-band and  $\text{P}^+/\text{v}(\pi)/\text{N}^+$  HOT FPAs.

**Acknowledgments** This work is supported by the Kunming Institute of Physics. The authors wish to thank all of their colleagues at the Kunming Institute of Physics who have worked together on the development of the HgCdTe described in this paper.

**Funding** Funding is provided by the National Key Research and Development Program of China (No. SQ2020YFB200190).

**Conflict of interest** The authors declare that they have no conflict of interest.

## References

1. C. Junhao, *Narrow-Gap Semiconductor Physics* (Beijing: Science Press, 2005).
2. Y. Jianrong, *Physics and Technology of HgCdTe Materials* (Beijing: National Defense Industry Press, 2012).

3. A. Rogalski, J. Antoszewski, and L. Faraone, Third-generation infrared photodetector arrays. *J. Appl. Phys.* 105(9), 4 (2009).
4. A. Rogalski, New material systems for third generation infrared detectors, in *Ninth International Conference on Correlation Optics, SPIE*, 7388, 178–189 (2009).
5. P.S. Wijewarnasuriya, P.Y. Emelie, A. D'Souza, G. Brill, M.G. Stapelbroek, S. Velicu, Y. Chen, C. Grein, S. Sivananthan, and N.K. Dhar, Nonequilibrium operation of arsenic diffused long-wavelength infrared HgCdTe photodiodes. *J. Electron. Mater.* 37(9), 1283–1290 (2008).
6. D. Lee, M. Carmody, E. Piquette, P. Dreiske, A. Chen, A. Yulius, D. Edwall, S. Bhargava, M. Zandian, and W.E. Tennant, High-operating temperature HgCdTe: a vision for the near future. *J. Electron. Mater.* 45(9), 4587–4595 (2016).
7. P. Madejczyk, W. Gawron, A. Kęblowski, K. Mlynarczyk, D. Stepien, P. Martyniuk, A. Rogalski, J. Rutkowski, and J. Piotrowski, Higher operating temperature IR detectors of the MOCVD grown HgCdTe heterostructures. *J. Electron. Mater.* 49(11), 6908–6917 (2020).
8. D. Lee, P. Dreiske, J. Ellsworth, R. Cottier, A. Chen, S. Tallarico, A. Yulius, M. Carmody, E. Piquette, M. Zandian, and S. Douglas, Law 19: the ultimate photodiode performance metric. *Proc. SPIE* 11407, 114070X–X114071 (2020).
9. M. Kopytko, and A. Rogalski, New insights into the ultimate performance of HgCdTe photodiodes. *Sens. Actuators A* 339, 113511 (2022).
10. E.P.G. Smith, G.M. Venzor, A.M. Gallagher, M. Reddy, J.M. Peterson, D.D. Lofgreen, and J.E. Randolph, Large-format HgCdTe dual-band long-wavelength infrared focal-plane arrays. *J. Electron. Mater.* 40(8), 1630–1636 (2011).
11. D.R. Rhiger, and J.W. Bangs, Current-voltage analysis of dual-band n-p-n HgCdTe detectors. *J. Electron. Mater.* 51(7), 4721–4730 (2022).
12. M. Carmody, D. Lee, M. Zandian, J. Phillips, and J. Arias, Threading and misfit-dislocation motion in molecular-beam epitaxy-grown HgCdTe epilayers. *J. Electron. Mater.* 32(7), 710–716 (2003).
13. H.F. Schaake, and A.J. Lewis, Electrically active defects in cid imaging arrays fabricated on  $\text{Hg}_{0.7}\text{Cd}_{0.3}\text{Te}$ . *MRS Online Proc. Libr. (OPL)*. 14, 301 (1983).
14. J.S. Chen, Etchant for revealing dislocations in II–VI compounds. U.S. Patent. 4,897,152 (1990-1-30).
15. J.R. Yang, X.L. Cao, Y.F. Wei, and L. He, Traces of HgCdTe defects as revealed by etch pits. *J. Electron. Mater.* 37(9), 1241–1246 (2008).
16. M. Reddy, J.M. Peterson, T. Vang, J.A. Franklin, M.F. Vilela, K. Olsson, E.A. Patten, W.A. Radford, J.W. Bangs, L. Melkonian, E.P.G. Smith, D.D. Lofgreen, and S.M. Johnson, Molecular beam epitaxy growth of HgCdTe on large-area Si and CdZnTe substrates. *J. Electron. Mater.* 40(8), 1706–1716 (2011).
17. M. Reddy, D.D. Lofgreen, K.A. Jones, J.M. Peterson, W.A. Radford, J.D. Benson, and S.M. Johnson, Cross-sectional study of macrodefects in MBE dual-band HgCdTe on CdZnTe. *J. Electron. Mater.* 42(11), 3114–3118 (2013).
18. B. Shojaei, R. Cottier, D. Lee, E. Piquette, M. Carmody, M. Zandian, and A. Yulius, Full-wafer strain and relaxation mapping of  $\text{Hg}_{1-x}\text{Cd}_x\text{Te}$  multilayer structures grown on  $\text{Cd}_{1-y}\text{Zn}_y\text{Te}$  substrates. *J. Electron. Mater.* 48(10), 6118–6123 (2019).
19. F.E. Arkun, D.D. Edwall, J. Ellsworth, S. Douglas, M. Zandian, and M. Carmody, Characterization of HgCdTe films grown on large-area CdZnTe substrates by molecular beam epitaxy. *J. Electron. Mater.* 46(3), 5374–5378 (2017).
20. M. Reddy, J.M. Peterson, F. Torres, B.T. Fennel, X. Jin, K. Doyle, T. Vang, N. Juanko, S.M. Johnson, and A. Hampp, Multi-wafer growth simultaneously on four 6 cm × 6 cm CdZnTe substrates for step increase in MBE HgCdTe wafer production. *J. Electron. Mater.* 51(7), 4758–4762 (2022).
21. S.M. Johnson, D.R. Rhiger, J.P. Rosbeck, J.M. Peterson, S.M. Taylor, and M.E. Boyd, Effect of dislocations on the electrical and optical properties of long-wavelength infrared HgCdTe photovoltaic detectors. *J. Vac. Sci. Technol. B Microelectron. Nanometer Struct. Process. Meas. Phenom.* 10(4), 1499–1506 (1992).
22. R.D. Rajavel, D.M. Jamba, O.K. Wu, J.E. Jensen, J.A. Wilson, E.A. Patten, K. Kosai, P. Goetz, G.R. Chapman, and W.A. Radford, High performance HgCdTe two-color infrared detectors grown by molecular beam epitaxy. *J. Cryst. Growth* 175, 653–658 (1997).
23. P. Lamarre, C. Fulk, D. D'Orsogna, E. Bellotti, F. Smith, P. Lovicchio, M.B. Reine, T. Parodos, J. Marciniak, S.P. Tobin, and J. Markunas, Characterization of dislocations in HgCdTe heteroepitaxial layers using a new substrate removal technique. *J. Electron. Mater.* 38(8), 1746–1754 (2009).
24. E.P.G. Smith, L.T. Pham, G.M. Venzor, E.M. Norton, M.D. Newton, P.M. Goetz, V.K. Randall, A.M. Gallagher, G.K. Pierce, E.A. Patten, R.A. Coussa, K. Kosai, W.A. Radford, L.M. Giegerich, J.M. Edwards, S.M. Johnson, S.T. Baur, J.A. Roth, B. Nosh, T.J. De Lyon, J.E. Jensen, and R.E. Longshore, HgCdTe focal plane arrays for dual-color mid-and long-wavelength infrared detection. *J. Electron. Mater.* 33(6), 509–516 (2004).
25. J.B. Varesi, A.A. Buell, J.M. Peterson, R.E. Bornfreund, M.F. Vilela, W.A. Radford, and S.M. Johnson, Performance of molecular-beam epitaxy-grown midwave infrared HgCdTe detectors on four-inch Si substrates and the impact of defects. *J. Electron. Mater.* 32(7), 661–667 (2003).
26. M.F. Vilela, K.R. Olsson, E.M. Norton, J.M. Peterson, K. Rybnicek, D.R. Rhiger, C.W. Fulk, J.W. Bangs, D.D. Lofgreen, and S.M. Johnson, High-performance M/LWIR dual-band HgCdTe/Si focal-plane arrays. *J. Electron. Mater.* 42(11), 3231–3238 (2013).
27. L. He, Y. Wu, L. Chen, M. Yu, J. Wu, J. Yang, Y. Li, R. Ding, and Q. Zhang, Progress in MBE growth of HgCdTe @ SITP. *Proc. SPIE* 4795, 17–26 (2002).
28. D.R. Rhiger, S. Sen, J.M. Peterson, H. Chung, and M. Dudley, Lattice mismatch induced morphological features and strain in HgCdTe epilayers on CdZnTe substrates. *J. Electron. Mater.* 26(6), 515–523 (1997).
29. C.L. Jiao, S.R. Zhao, X.Q. Chen, and Y.F. Wei, The relationship of lattice mismatch the HgCdTe/CdZnTe with x-ray diffraction. *Laser Infrared* 37, 910–914 (2007).
30. Y. Chang, C.R. Becker, C.H. Grein, J. Zhao, C. Fulk, T. Caselman, R. Kiran, X.J. Wang, E. Robinson, S.Y. An, S. Mallick, S. Sivananthan, T. Aoki, C.Z. Wang, D.J. Smith, S. Velicu, J. Zhao, J. Crocco, Y. Chen, G. Brill, P.S. Wijewarnasuriya, N. Dhar, R. Sporken, and V. Nathan, Surface morphology and defect formation mechanisms for HgCdTe (211) B grown by molecular beam epitaxy. *J. Electron. Mater.* 37(9), 1171–1183 (2008).
31. E.C. Piquette, M. Zandian, D.D. Edwall, and J.M. Arias, MBE growth of HgCdTe epilayers with reduced visible defect densities: kinetics considerations and substrate limitations. *J. Electron. Mater.* 30(6), 627–631 (2001).
32. I.V. Sabinina, A.K. Gutakovskiy, Yu.G. Sidorov, and A.V. Latyshev, Nature of V-shaped defects in HgCdTe epilayers grown by molecular beam epitaxy. *J. Cryst. Growth* 274(3–4), 339–346 (2005).
33. M. Reddy, W.A. Radford, D.D. Lofgreen, K.R. Olsson, J.M. Peterson, and S.M. Johnson, Study of morphological defects on dual-band HgCdTe on CdZnTe. *J. Electron. Mater.* 43(8), 2991–2997 (2014).
34. M. Reddy, J. Wilde, J.M. Peterson, D.D. Lofgreen, and S.M. Johnson, Study of macrodefects in MBE-Grown HgCdTe epitaxial layers using focused ion beam milling. *J. Electron. Mater.* 41(10), 2957–2964 (2012).

35. M.A. Kinch, The future of infrared; III–Vs or HgCdTe? *J. Electron. Mater.* 44(9), 2969–2976 (2005).
36. D. Eich, W. Schirmacher, S. Hanna, K.M. Mahlein, P. Fries, and H. Figgemeier, Progress of MCT detector technology at AIM towards smaller pitch and lower dark current. *J. Electron. Mater.* 46(9), 5448–5457 (2017).
37. L. Rubaldo, A. Brunner, P. Guinedor, R. Taalat, J. Berthoz, D. Sam-Giao, L. Dargent, N. Péré-Laperne, V. Chaffraix, M.L. Bourqui, Y. Loquet, and J. Coussement, Recent advances in Sofradir IR on II–VI photodetectors for HOT applications. *Quantum Sens. Nano Electron. Photonics XIII*. 9755, 157–170 (2016).

**Publisher's Note** Springer Nature remains neutral with regard to jurisdictional claims in published maps and institutional affiliations.

Springer Nature or its licensor (e.g. a society or other partner) holds exclusive rights to this article under a publishing agreement with the author(s) or other rightsholder(s); author self-archiving of the accepted manuscript version of this article is solely governed by the terms of such publishing agreement and applicable law.